12th IEA Heat Pump Conference 2017

Dynamic Characteristics of an R-410A Multi-split Variable Refrigerant Flow Air-conditioning System

Hongtao Qiao*, Christopher R. Laughman, Daniel J. Burns, Scott A. Bortoff

Mitsubishi Electric Research Laboratories
Cambridge, MA 02139, USA

Abstract

Multi-split variable refrigerant flow (VRF) air-conditioning systems, composed of a single outdoor heat exchanger and multiple indoor heat exchangers, are becoming increasingly popular because of the ease with which they can be installed, their high energy savings potential, and the opportunity to realize individualized comfort control. Because these systems exhibit strong coupling effects between different indoor units, coordinated control of compressor speed, fan speeds, and valve openings is required. A literature review indicates there is a dearth of comprehensive studies that explore the complex multivariable dynamic behavior of air-source VRF systems with commercially prevalent architectures. This paper describes a first-principles model of such an air-conditioner with four indoor units that is validated against experimental data. This validated simulation model is then used to study the dynamic system response subject to various sets of conditions, including variations in the compressor speed, fan speeds, and valve openings. The insights gained from such a system analysis will be beneficial to future energy performance analysis and model-based controls design.

Selection and/or peer-review under responsibility of the organizers of the 12th IEA Heat Pump Conference 2017.

Keywords: modeling; dynamic simulation; multi-split; variable refrigerant flow; air-conditioning

Nomenclature

Symbols

A	area [m^2]	q	heat transfer rate [W]
c_p	specific heat [J kg^{-1} K^{-1}]	q''	heat flux [W m^{-2}]
C_v	flow coefficient [-]	t	time [s]
f	frequency [Hz]	T	temperature [K]
G	mass flux [kg m^{-2}]	u	velocity [m s^{-1}]
h	specific enthalpy [J kg^{-1}]	V	volume [m^3]
$\dot{m}$	mass flow rate [kg s^{-1}]	$\dot{V}$	volumetric flow rate [m^3 s^{-1}]
M	mass [kg]	$\dot{W}$	power [W]
p	pressure [Pa]	x	flow quality [-]
P	perimeter [m]	$\hat{x}$	static quality [-]

* Corresponding author. Tel.: +1-617-621-7586; fax: +1-617-621-7550.
E-mail address: qiao@merl.com.

Greek letters

α	heat transfer coefficient [W m^{-2} K^{-1}] or mass transfer coefficient [kg s^{-1} m^{-2}]	ρ	density [kg m^{-3}]
λ	fraction of power absorbed by compressor [-]	τ	wall shear stress [N m^{-1}]
φ	pressure ratio [-]	ϖ	frequency ratio [-]
γ	void fraction [-]	ω	humidity ratio [kg H_2O / kg dry air]
η	efficiency [-]		

Subscripts

a	air	nom	nominal
dis	discharge	o	external
disp	displacement	out	outlet
f	saturated liquid	r	refrigerant
fg	liquid to gas	sat	saturation
fin	fin	suc	suction
g	saturated vapor	t	tube
in	inlet	w	wall

1. Introduction

Multi-split VRF systems are becoming increasingly popular due to their high energy saving potential and the capability of separately controlling the conditions in individual zones. A typical VRF air conditioning system, as shown in Figure 1, has a single outdoor unit and multiple indoor units. The outdoor unit incorporates a variable speed compressor, an accumulator, and a condenser-fan coil, whereas each indoor unit encompasses an electronic expansion valve (EEV), an evaporator coil, and an air circulating blower. The dynamics of these systems are more complex than those of conventional variable air volume (VAV) systems with a single evaporator because the coupling between the outdoor unit and all of the indoor units may cause the operation of the indoor unit in one zone to influence the operation of the indoor units in other zones.

Both experimental and simulation studies have been extensively reported in the literature to explore the operating characteristics and controls design of VRF systems. Park *et al.* [1] simulated the performance of a multi-type air conditioner with two evaporators and concluded that the major control parameter of the system that can be used to regulate different space conditions is the EEV opening. Choi and Kim [2] conducted a series of experimental studies to examine the capacity modulating characteristics of a VRF system in steady-state under various operating conditions. They found that the behavior of the different indoor units are strongly coupled. Shah *et al*. [3] presented a generalized dynamic modeling approach for multi-evaporator air-conditioning systems sized for mobile and automotive applications, and also experimentally observed a strong coupling effect between different evaporators. Chiou *et al*. [4] applied a fuzzy control method to VRF systems using fixed-orifice expansion devices to experimentally achieve temperature regulation for two conditioned zones. Shao *et al*. [5] also developed and validated a dynamic model with a two-phase fluid network to investigate the transient characteristics of multi-unit air conditioners by varying the compressor speed and EEV orifice sizes. Finally, Yan *et al*. [6] performed a modeling study to investigate the effect of refrigerant pipeline length on the steady-state operational performance of a two evaporator air conditioning system.

While the cited body of work provides insight into the performance of and controls design for a variety of VRF system types, there are few publications that present experimentally validated models which adequately capture the transient heat transfer and fluid flow characteristics of commercially available air-source VRF systems that are commonly installed in contemporary buildings. One motivation of this paper is the development of an experimentally-validated first-principles model for a VRF air conditioning system with four indoor units, sized for a typical residential application, which will facilitate the exploration of system dynamics via simulation.

As highlighted by even this brief literature survey, one of the distinctive characteristics of VRF systems is the behavior related to the refrigerant-side coupling between the evaporators. The effects of this coupling must be mitigated in successful controller designs to allow users in separate spaces to maintain independent control of their thermal comfort. Similar coupling phenomena are also encountered in multi-evaporator commercial refrigeration systems, which are consequently often equipped with pressure regulating valves (PRVs) at each evaporator exit to decouple the evaporator dynamics and allow each evaporator to operate at a separate saturation pressure. While

some literature [7] studies analogous approaches for air-conditioning applications, the evaporators in most common VRF systems are directly connected via a common manifold to avoid the use of these PRVs. Such a system structure makes it difficult to maintain different evaporating temperatures, and also increases the degree of coupling between evaporators. In Jain *et al.* [8], the authors address this challenge by proposing a partially decentralized controller design for VRF systems that relies upon the pressure drop across the pipes connecting the evaporator outlets to dynamically decouple the individual evaporating pressures. This approach was only evaluated in simulation, however, and its efficacy was not demonstrated experimentally. Accordingly, the second objective of this paper involves the use of these dynamic models to study the influence of these pipe lengths on the system dynamics and thereby better understand the robustness of such decentralized control strategies for systems that are commonly sold today.

The paper is organized as follows. In Section 2, we first derive dynamic models for all the components in the system. These models are then validated and the dynamic system response due to a variety of time-varying inputs is studied in Section 3. In Section 4, we discuss the influence of the pipeline lengths on the coupling of evaporating pressures. Conclusions from this work are then summarized in Section 5.

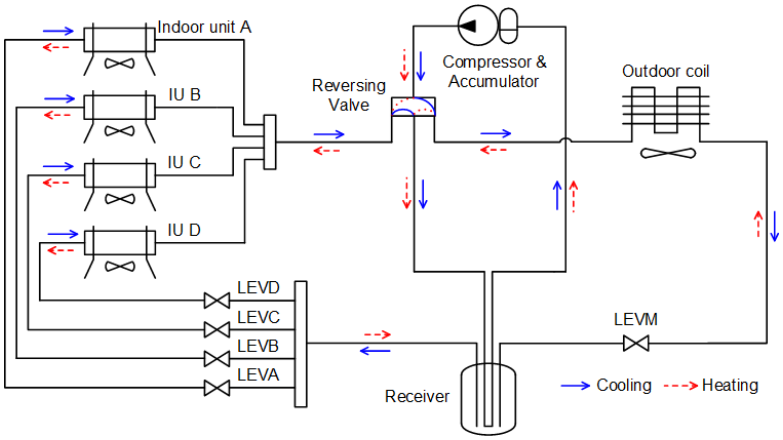

Fig. 1. Schematic of a VRF System with Four Indoor Units

2. Model Development

2.1. Compressor Model

A variable-speed high-side rotary compressor, in which the motor is cooled by compressed high-pressure discharge refrigerant, was used in this work. Because the performance map for these compressors has reduced accuracy when extrapolated beyond the specific ranges of saturated discharge and suction temperatures over which it is tabulated, we converted the performance map into a set of curve-fitted equations to avoid poor numerical behavior during the simulations.

The volumetric efficiency of this compressor model is a function of the suction pressure, discharge pressure and compressor frequency

$$\eta_v = \kappa_0 + \kappa_1\varphi + \kappa_2\varphi^2 + \kappa_3\left(p_{dis} - p_{suc}\right)\left(1+\kappa_4 p_{suc}\right), \tag{1}$$

where $\varphi = p_{dis}/p_{suc}$, $\kappa_i = a_{i,1} + a_{i,2}\varpi + a_{i,3}\varpi^2$, and $\varpi = f/f_{nom}$. The power consumed by the compressor is determined by

$$\dot{W} = \zeta_1 p_{suc}\dot{V}_{suc}\left(\varphi^{\zeta_2} - \zeta_3\right) + \zeta_4, \tag{2}$$

where $\zeta_i = b_{i,1} + b_{i,2}\varpi + b_{i,3}\varpi^2$. In addition, the fraction of the compressor power absorbed by the refrigeration is determined by

$$\lambda = \theta_0 + \theta_1\varphi + \theta_2\varphi^2, \tag{3}$$

where $\theta_i = c_{i,1} + c_{i,2}\varpi + c_{i,3}\varpi^2$. Lastly, the mass flow rate delivered by the compressor is determined by

$$\dot{m} = \eta_v f \rho_{suc} V_{disp}, \tag{4}$$

and the enthalpy of the discharged refrigerant is

$$h_{dis} = \lambda\dot{W}/\dot{m} + h_{suc}. \tag{5}$$

2.2. Expansion Valve Model

Linear electronic expansion valves (LEVs) were also used in the system. A standard orifice-type relationship between mass flow rate and pressure drop across the valve was used to describe the system behavior, in which the mass flow rate through the valve is determined by the flow coefficient, the inlet density, and the pressure difference across the valve

$$\dot{m} = C_v \sqrt{\rho_{in} \Delta p} \,, \tag{6}$$

where the flow coefficient C_v is a function of the valve opening determined by regression based on experimental data.

2.3. Receiver and Accumulator Models

Both the receiver and accumulator were modeled as lumped control volumes with one inlet and one outlet by adopting the following simplifications: (1) ideal phase separation, (2) vapor and liquid in the tank are in thermodynamic equilibrium, (3) pressure drop inside the tank is negligible, and (4) the tank is adiabatic. Under these assumptions, the governing equations for the refrigerant dynamics are as follows:

$$V \frac{d\bar{\rho}}{dt} = \dot{m}_{in} - \dot{m}_{out} \,, \tag{7}$$

$$V\left(\bar{\rho} \frac{d\bar{h}}{dt} - \frac{dp}{dt} \right) = \dot{m}_{in} \left(h_{in} - \bar{h} \right) - \dot{m}_{out} \left(h_{out} - \bar{h} \right). \tag{8}$$

In this model, the enthalpy of the fluid leaving the tank is dependent upon the mean state of the refrigerant inside the tank. The model must take into account two different operational cases into account, in which the state of the refrigerant inside the tank is either single-phase or two-phase. In the single-phase case, the enthalpy of the outlet stream is set equal to the mean enthalpy of the refrigerant in the tank; in the two-phase case, the enthalpy of the outlet stream is determined depending upon whether the outlet is fully submerged, partially submerged or not submerged.

2.4. Heat Exchanger and Pipe Models

The heat exchangers were described by a finite-volume model of the heat and fluid flow. Each heat exchanger segment is divided into three sections: the refrigerant stream, the finned walls, and the air stream. The refrigerant stream is described by a one-dimensional flow with fluid properties varying only in the direction of flow; consequently, these properties are uniform or averaged at every cross section along the axis of the channel. Additional assumptions used to simplify the dynamic models included: (1) the fluid is Newtonian, (2) axial heat conduction in the direction of refrigerant flow is ignored, (3) viscous dissipation is neglected, (4) liquid and vapor are in thermodynamic equilibrium in each volume in the two-phase region, (5) the potential energy and kinetic energy of the refrigerant are neglected, and (6) dynamic pressure waves are of minor importance and are thus neglected in the momentum equation. The conservation laws can thus be formulated as follows:

$$\frac{\partial}{\partial t}\left(\bar{\rho} A \right) + \frac{\partial}{\partial z}\left(GA \right) = 0 \tag{9}$$

$$\frac{\partial}{\partial t}\left(\bar{\rho} \bar{h}_\rho A \right) + \frac{\partial}{\partial z}\left(G\bar{h}A \right) = Pq_w'' + \frac{\partial}{\partial t}\left(pA \right) \tag{10}$$

$$A\frac{\partial p}{\partial z} + \bar{\tau}_w P = 0 \,, \tag{11}$$

where average density, average mass flux, average density-weighted enthalpy, average flow-weighted enthalpy, average wall shear stress are defined as follows, respectively.

$$\bar{\rho} = \frac{1}{A}\int_A \rho dA \,,\ G = \frac{1}{A}\int_A \rho u dA \,,\ \bar{h}_\rho = \frac{1}{\bar{\rho}}\left(\frac{1}{A}\int_A \rho h dA \right),\ \bar{h} = \frac{1}{G}\left(\frac{1}{A}\int_A \rho u h dA \right),\ \bar{\tau}_w = \frac{1}{P}\int_P \tau_w dl \,.$$

For single-phase flow, the refrigerant density can be presumed to be uniform at each cross sectional area, and the following relations can be readily obtained

$$\bar{\rho} = \rho \tag{12}$$

$$\bar{h}_\rho = \bar{h} = h. \tag{13}$$

This work relaxed the typical homogeneous flow assumption of equality between the velocities of vapor and liquid for control volumes in the two-phase region to achieve a more realistic refrigerant system mass inventory for the overall system. This necessitated the use of the average density and specific enthalpies for two-phase flow, which are determined by

$$\bar{\rho} = \rho_g \gamma + \rho_f (1-\gamma) \tag{14}$$

$$\bar{h}_\rho = \left[\rho_g h_g \gamma + \rho_f h_f (1-\gamma) \right] / \bar{\rho} \tag{15}$$

$$\bar{h} = \left[\rho_g u_g h_g \gamma + \rho_f u_f h_f (1-\gamma) \right] / G = h_g x + h_f (1-x), \tag{16}$$

where the void fraction and flow quality are defined as

$$\gamma = \frac{\text{area of gas}}{\text{total area}} = \frac{A_g}{A_g + A_f} = \frac{A_g}{A}, \text{ and} \tag{17}$$

$$x = \frac{\text{mass flow of gas}}{\text{total mass flow}} = \frac{\rho_g u_g \gamma}{\rho_g u_g \gamma + \rho_f u_f (1-\gamma)} = \frac{\rho_g u_g \gamma}{G}. \tag{18}$$

The flow quality x is distinct from the static quality $\hat{x}$, which is defined as the ratio of mass of vapor to that of the total mixture,

$$\hat{x} = \frac{M_g}{M_g + M_f} = \frac{\rho_g \gamma}{\rho_g \gamma + \rho_f (1-\gamma)}. \tag{19}$$

Hence, the density-weighted enthalpy can be described using the static quality

$$\bar{h}_\rho = \hat{x} h_g + (1-\hat{x}) h_f. \tag{20}$$

The pressures and density-weighted enthalpies of each control volume are used as the state variables in the heat exchanger model. Density-weighted enthalpy can be related to flow-weighted enthalpy via

$$\bar{h} - \bar{h}_\rho = (x - \hat{x})(h_g - h_f). \tag{21}$$

Note that x and $\hat{x}$ are both zero for the subcooled liquid and unity for the superheated vapor, implying that these two enthalpies should be equal to each other for single-phase flows. All of the variables in Equation (21) are thermodynamic properties, and can be readily calculated except for the flow quality x. In this work, the flow quality was obtained by using the Zivi slip-ratio based void fraction model [9] because of its simplicity.

While this refrigerant-side model was principally developed for the heat exchangers, it was also used to describe the behavior of the refrigerant pipes connecting the components. These pipe models were an important part of the overall system model because they contained a significant fraction of the refrigerant in the entire system. The main distinction between the pipe models and the heat exchanger models regards the air-side models used: the heat exchanger air-side models describe the effect of the enhanced heat transfer surface, while the pipe air-side models use natural convection as the boundary condition.

The model of the air-side of the heat exchanger is based on the following assumptions: (1) one-dimensional quasi-steady airflows, (2) negligible heat conduction in direction of the air flow, (3) the temperature profile within fins follows the steady-state profile, allowing the use of heat transfer and combined heat and mass transfer fin efficiencies, (4) simultaneous heat and mass transfer follows the Lewis analogy, and (5) equal temperature of tube wall and fins within each control volume. Under these assumptions, the governing equations for the air side describing the energy balances for the wetted coils are

$$\dot{m}_a c_{p,a} \frac{dT_a}{dy} \Delta y = \alpha_a \left(A_{o,t} + \eta_{fin} A_{o,fin} \right) (T_w - T_a) \tag{22}$$

$$\dot{m}_a \frac{d\omega_a}{dy} \Delta y = \alpha_m \left(A_{o,t} + \eta_{fin} A_{o,fin} \right) \min\left(0, \omega_{w,sat} - \omega_a \right), \tag{23}$$

where $\omega_{w,sat}$ is the humidity ratio of saturated air evaluated at T_w. The mass transfer coefficient α_m is determined by applying the Lewis analogy.

Finally, without considering the axial conduction along the tube, the energy equation of the tube walls and associated fins can be written as

$$\left(M_t c_{p,t} + M_{fin} c_{p,fin}\right)\frac{dT_w}{dt} = q_r + q_a \tag{24}$$

$$q_r = \alpha_r A\left(T_r - T_w\right) \tag{25}$$

$$q_a = \dot{m}_a\left[c_{p,a}\left(T_{a,in} - T_{a,out}\right) + \left(\omega_{a,in} - \omega_{a,out}\right)\Delta h_{fg}\right]. \tag{26}$$

2.5. Implementation

The above models describing the balance equations were augmented by a set of empirical closure relations describing the single- and two-phase heat transfer coefficients and frictional pressure drops for the fluid on both the refrigerant side and the air-side. When implementing these models in the simulation environment, a tube-by-tube analysis is employed for the heat exchangers, i.e., performance of each tube is analyzed separately and each tube is associated with different refrigerant parameters and air mass flow rate, inlet temperature and humidity.

These models were implemented in the Modelica language using the Dymola 2017 [10] simulation environment, while the refrigerant property models for R-410A were obtained from the Vapor Cycle Library v. 1.3 [11], which used the pseudo-pure formulation of Lemmon [12]. Modelica was well suited to this effort as an object-oriented equation-based acausal modeling language because it facilitated the independent development of detailed physical models of each of the components which could then be interconnected to form a complete system model. These models were compiled and run on a laptop with an Intel i7 processor with 8 Gb of RAM; the DASSL solver was used to integrate the set of differential algebraic equations with a tolerance of 10^{-5}.

3. Simulation Results and Experimental Validation

To evaluate the efficacy of these models, we calibrated them against experimental data collected from a commercially-available multi-evaporator air-conditioning system and compared the simulation output to the experimentally measured data. A 4 indoor unit variable-speed multi-split heat pump system with a cooling capacity of 48 kBTU/h was constructed in our laboratory and fully instrumented to obtain detailed information about its dynamic behavior. This system was installed in a set of test chambers with internal volumes of approximately 9 m^3 that were built from 4″ foam insulation, which enabled us to manage the boundary conditions on the air-conditioning system. A secondary water-based heating and cooling system regulated the air temperature at the outdoor unit and the heat loads for the indoor units to maintain control of the boundary conditions.

Four experiments were conducted to validate the simulation results: (1) step change in compressor speed, (2) step change in LEV opening, (3) step change in outdoor fan speed, and (4) step change in indoor fan speed. These tests were all conducted for an open-loop system to avoid dynamics related to the closed-loop controls. Before conducting any step change experiments, we started the system with the same set of initial conditions and actuator inputs and operated it for approximately 3 hours to until the dynamics caused by the start-up transient died out. The set of initial system inputs is provided in Table 1.

Table 1. Initial experimental system inputs

System input	Value	Units
Indoor/Outdoor chamber temperature	22/35	°C
Indoor/Outdoor chamber relative humidity	60%/50%	-
Compressor frequency	75	Hz
LEV opening (A, B, C & D)	14%, 14%, 16% & 16%	-

3.1. Compressor Speed Step Response

The first set of step responses examined were obtained by first stepping the compressor speed from its initial value of 75 Hz to the new value of 83 Hz, and then allowing the system to reach a new steady-state operating point. The resulting pressure, temperature, and mass flow rate transients are illustrated in Figure 2, and demonstrate good correspondence between the output of the simulations and the experimentally obtained data, with steady-state discrepancies of 3%, 2% and 1% for pressures, temperatures and mass flow rate, respectively.

Suction and discharge pressure transients for the step-up change in the compressor speed are shown in Figure

2a; increased compressor speed caused a 6.5% reduction in the suction pressures due to the lower refrigerant inventory in the evaporator, as well as a 3.6% increase in the discharge pressures due to the higher refrigerant inventory in the condenser. Similarly, the suction and discharge temperature waveforms for the same increase in compressor speed are shown in Figure 2b. The suction temperature exhibits no observable change in the vicinity of the compressor step, due to the opposing effects of the reduced suction temperature and the increased refrigerant mass flow rate; the former tends to increase the suction superheat for relatively small changes in the compressor speed, while the latter tends to decrease the suction superheat. In comparison, the discharge temperature shows an 8K increase during the compressor speed step, due to the increased power consumption. Refrigerant mass flow rate, in particular, rises abruptly after the increase in compressor speed because of the correspondingly rapid increase in the compressor speed in the face of the relatively slow system dynamics. The mass flow rate then decreased after the initial surge as the disturbance propagated through the system, which increased the pressure ratio until the system reached a new steady-state operating point.

3.2. LEV Opening Step Response

During this transient, the LEV position of the indoor unit D was reduced from 16% to 12%, while the LEVs of the indoor units A, B, and C maintained their positions at 14%, 14% and 16%, respectively. The resulting pressure, temperature and mass flow rate transients are illustrated in Figure 3, and again show a good match between the simulation and the experiment, with the steady-state discrepancies of 3%, 2% and 1% for pressures, temperatures and mass flow rate, respectively.

A resulting 7.5% drop in the suction pressure can be observed in Figure 3a, due to the lower mass inventory in the evaporator that results from the reduced refrigerant mass flow rate. This lower suction pressure is related to both reduced suction density and reduced refrigerant mass flow rate; the effect of this lower pressure difference across the LEVs required to balance the lower refrigerant mass flow rate is manifested as a 5.3% decline the discharge pressure as the system reaches a new steady-state operating point. In comparison, Figure 3b illustrates relatively constant suction and discharge temperatures during the change in LEV position. Since the change in the position of LEV D resulted in an increased suction superheat but a decreased evaporating pressure, the suction pressure remains nearly constant. Similarly, the strong correlation between discharge temperature and compressor speed suggests that the relatively constant discharge temperature is related to the constant compressor speed.

3.3. Fan Speed Step Responses

We first studied the system dynamics resulting from changes to the outdoor fan speed by increasing it from 700 rpm to 1000 rpm, and then changing it back to 700 rpm after the system had reached steady-state; the resulting transients of pressures, temperatures and refrigerant mass flow are shown in Figure 4. The models again exhibit behavior which is consistent with that of the experiments, with the steady-state discrepancies of 2%, 2% and 2% for pressures, temperatures and mass flow rate, respectively; additional support for the fidelity of the model can also be obtained from the fact that the system dynamics during the step down in fan speed are opposite of those exhibited during the step up in fan speed. The increased volumetric flow rate of air through the outdoor coil at the higher fan speed resulted in a higher air side heat transfer coefficient and a lower heat transfer temperature difference between refrigerant side and air side. Consequently, both the condensing pressure and discharge pressure decreased by 8.4%, while the suction pressure only declined by 3.9%, as shown in Figure 4a. This reduction in the pressure difference across the LEVs led to a 3.6% lower refrigerant flow rate, as shown in Figure 4b. In comparison with the almost stabilized suction temperature, the discharge temperature decreased by 5 K due to the lower power consumption of the compressor.

The effect of changing the indoor unit fan speed was also studied by varying the fan speed of indoor unit D between the highest and lowest values, while leaving the rest of the indoor unit fans at their highest value. As was the case for the outdoor unit fan speed, most of the simulation outputs and experimental data exhibit similar behavior for both the step down and step up in fan speed, with the steady-state discrepancies of 2%, 3% and 3% for pressures, temperatures and mass flow rate, respectively. While there is an observable mismatch between the simulated and experimental discharge temperatures, this can be attributed to the simplified compressor model, which does not account for the complex internal heat transfer between refrigerant and metallic surfaces in the compressor shell assembly. As is evident from the waveforms illustrated in Figure 5, the reduction in the volumetric air flow rate and air-side heat transfer coefficient that accompanied the change in the fan speed caused the refrigerant superheat at the outlet of the indoor unit D to diminish to the point that two-phase refrigerant eventually began to exit the evaporator, leading to a decline in both suction and discharge temperatures. This

change in fan speed also resulted in 35 kPa and 75 kPa reduction of suction and discharge pressures, respectively, due to the lower refrigerant flow rate caused by the reduction in the suction density.

4. Influence of Pipeline Length on Evaporating Pressure Coupling

As is evident from these models, the length of the pipe connecting the evaporators to the suction port of the compressor plays a critical role in the coupling between evaporator pressures. While the lengths of the pipes and their commensurate pressure losses impose important constraints on the steady-state values of the evaporating pressures, the dynamic effects of this coupling are less obvious and must be studied via dynamic simulation. We studied this coupling by first considering a case in which all four pipe lengths are 3 meters long, and simulated the behavior of these pipes by using the Blasius correlation [13] to describe the frictional pressure drop. We analyzed the coupling among evaporator pressures by linearizing the model derived in Section 2 about a steady-state operating point, and then computed the multivariable frequency response between the four LEVs and the four pressures across the pipes. The frequency response shown in Figure 6 is symmetric for the traces pertaining to identical pipe lengths (blue lines), with the diagonal elements showing the frequency response from LEV A and LEV D to pipe pressure drops 1 and 4, respectively, while the off-diagonal elements show the coupling between this pair of evaporators (the other frequency responses of other pairs are identical and are not shown). These frequency responses indicate that the off-diagonal gains are approximately 5-10 times smaller than the diagonal gains and that the system is diagonally dominant [14], suggesting that each LEV may be used to control the corresponding evaporator outlet pressure using standard decentralized control techniques, such as proportional-integral (PI) feedback control, without accounting for significant interaction and coupling between evaporators or risk of instability. The resulting closed-loop system will not be destabilized by the off-diagonal terms, and the dynamic coupling among pipe pressures is relatively small in this symmetric case.

In practice, however, the pipe lengths connecting the evaporators to the outdoor unit are seldom the same length, as they often serve different rooms that vary in distance from the outdoor unit. We therefore considered the case in which three of the pipe lengths (for evaporators A, B, and C) are 3m, and the pipe for evaporator D is 50m. We again compute the multivariable frequency response between the four LEVs and the four pipe pressures. The frequency responses corresponding to this unequal pipe length scenario are also shown in Figure 6 (red lines), and demonstrate strong interactions between LEV A and pipe pressure D, although the gain from LEV D to pipe pressure A remains small. This is characteristic of a so-called triangular system that has one-way coupling. In this case, we may still design a decentralized PI control for each subsystem by ignoring the coupling and expect to obtain a stable closed-loop system, as can be verified using the relative gain array or a structured singular value analysis [14]. However, the dynamic coupling from evaporator A to evaporator D is significant in both the open and closed loop. The effect of this coupling is illustrated in Figure 7, in which we designed 4 PI controllers to regulate each separate evaporator outlet pressure, and then applied a step to the closed evaporator A loop. As shown in the top plot in Figure 7, the evaporator A pressure across the return line responds quickly with little overshoot; unfortunately, this also produces a large disturbance to evaporator D, as shown in the bottom plot. This response is 4.3x the magnitude of the desired step change in evaporator A, as can be gleaned from inspection of the peak magnitude of the off-diagonal frequency response in Figure 6. This behavior is likely to be quite undesirable in practice, as the evaporator pressure transients (and thus evaporating temperature transients) in evaporator A are effectively amplified by 4x in evaporator D. This behavior cannot be compensated using higher feedback gains for evaporator D in a decentralized controller, but could be compensated with a feedforward term from the evaporator A loop to LEV D. Such robustness problems would likely persist, however, because the construction of this feedforward term would depend on the specific values of pipe lengths, and the controller would not be robust with respect to changes in this system parameter.

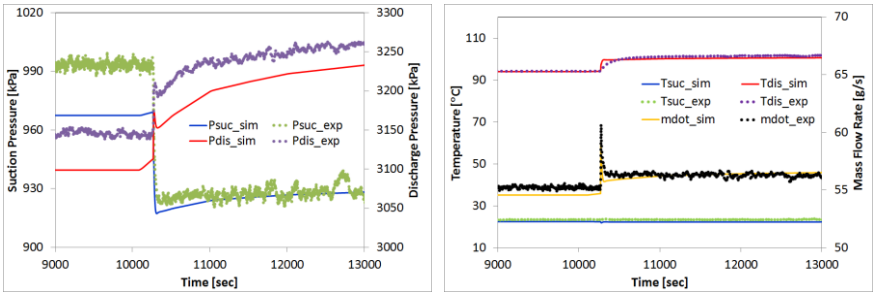

(a) (b)

Fig. 2. Compressor speed step response: (a) pressure response; (b) temperature & mass flow rate response

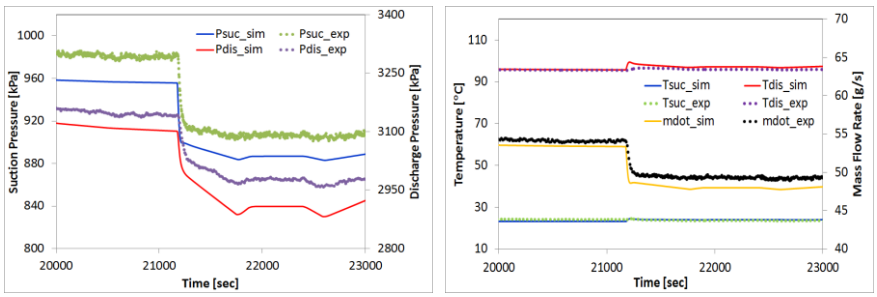

(a) (b)

Fig. 3. LEV D opening step response - (a) pressure response; (b) temperature & mass flow rate response

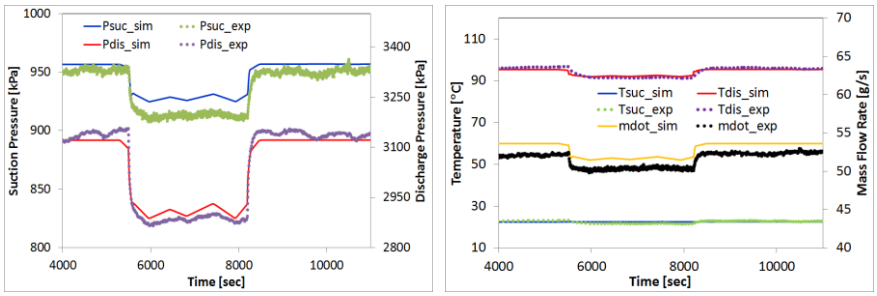

(a) (b)

Fig. 4. Outdoor fan speed response - (a) pressure response; (b) temperature & mass flow rate response

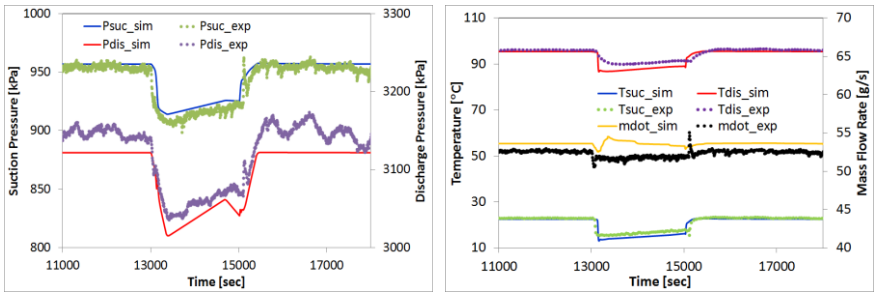

(a) (b)

Fig. 5. Indoor fan speed response - (a) pressure response; (b) temperature & mass flow rate response

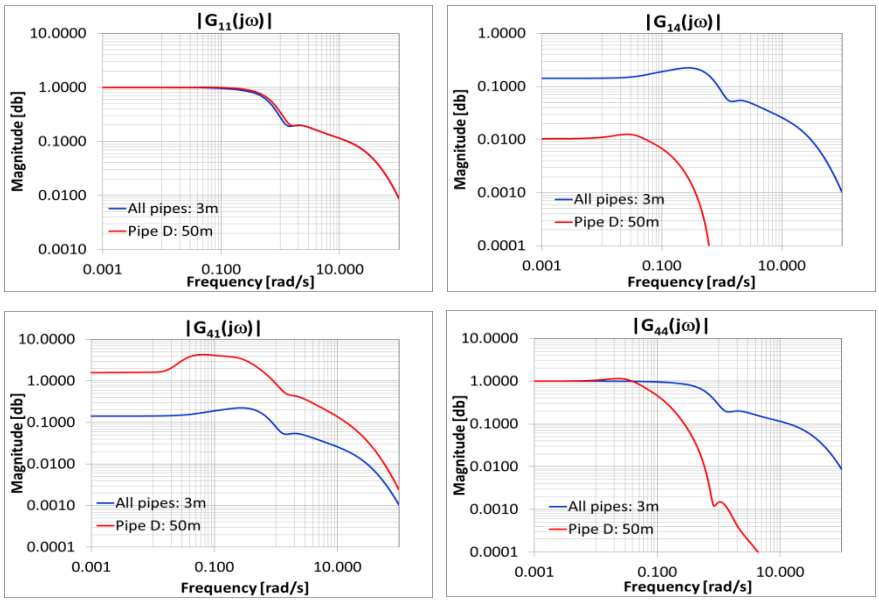

Fig. 6. Frequency response from LEVs to evaporator pipe pressures - blue lines: all pipe lengths are 10m; red lines: three pipe lengths (A,B,C) are 3m and D is 50m

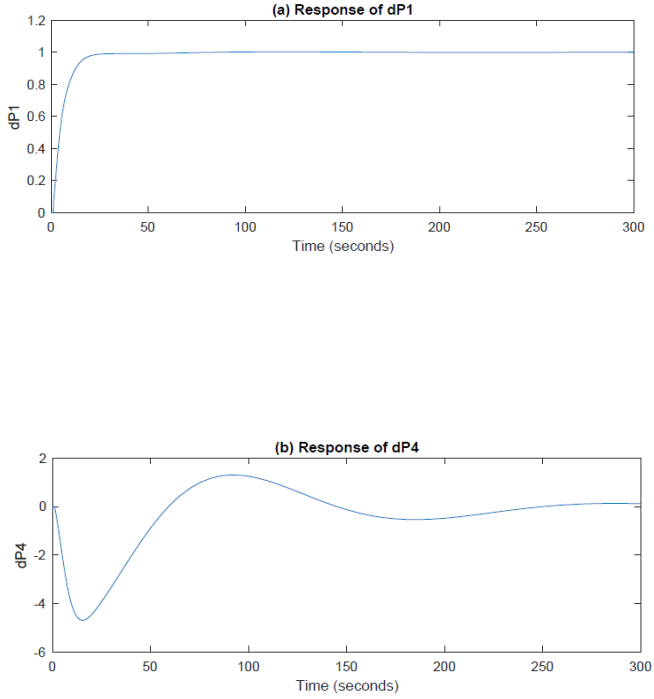

Fig. 7. Closed loop step response for decentralized PI control where evaporator (A,B,C) pipe lengths are 3m and pipe D length is 50m

5. Conclusions

Multi-split VRF systems exhibit more complex dynamics than conventional single-evaporator systems. In this paper, a dynamic model for a VRF system with four indoor units was developed. The heat exchangers were modeled with the finite volume method, whereas other components were described via a lumped-parameter models. The system model was validated against a series of experiments, and a comparison between simulation results and measurement data showed favorable agreement. The dynamic system response subject to various conditions was studied, and a strong coupling between different indoor units was observed. The effects of the coupling between the evaporator outlet pressures were also studied, we found that effect of differing line lengths significantly affected the transient behavior of the system. Information about such interactions will be invaluable when designing control systems that are robust to plant variations that are encountered in practice.

References

[1] Park YC, Kim YC, Min MK. Performance analysis on a multi-type inverter air conditioner. *Energ. Convers. Manage.* 2001; 42: 1607-21.
[2] Choi JM, Kim YC. Capacity modulation of an inverter-driven multi-air conditioner using electronic expansion valves. *Energy* 2003; 28: 141-55.
[3] Shah R, Alleyne AG, Bullard CW. Dynamic modeling and control of multi-evaporator air conditioning systems. *ASHRAE Trans.* 2004; 110 (Part 1): 109-19.
[4] Chiou CB, Chiou CH, Chu CM, Lin SL. The application of fuzzy control on energy saving for multi-unit room air-conditioners. *Appl. Therm. Eng.* 2009; 29: 310-16.
[5] Shao S, Xu H, Tian C. Dynamic simulation of multi-unit air conditioners based on two-phase fluid network model. *Appl. Therm. Eng.* 2012; 40: 378-88.

[6] Yan P, Xu X, Xia L, Deng S. A modelling study on the effects of refrigerant pipeline lengths on the operational performance of a dual-evaporator air conditioning system. *Appl. Therm. Eng.* 2012; 39: 15-25.
[7] Elliot MS, Rasmussen BP. Decentralized model predictive control of a multiple evaporator air conditioning system. *Control Eng. Pract.* 2013; 21: 1665-77.
[8] Jain N, Koeln JP, Sundaram S, Alleyne AG. Partially decentralized control of large-scale variable-refrigerant-flow systems in buildings. *J. Process Control* 2014; 24: 798-819.
[9] Zivi SM. Estimation of steady-state steam void-fraction by means of the principle of minimum entropy production. *J. Heat Trans-T ASME* 1964; 86: 247-52.
[10] AB Dassault Systemes. Dymola. 2016.
[11] Vapor Cycle Library. Modelon AB. 2016.
[12] Lemmon EW. Pseudo-pure fluid equations of state for the refrigerant blends R-410A, R404A, R507A, and R-407C. *Int. J. Thermophys.* 2003; 24: 991-1006.
[13] Incropera FP, DeWitt DP. Introduction to Heat Transfe, Third Edition. John Wiley & Sons, New York; 1996.
[14] Skogestad S, Postlethwaite I. Multivariable Feedback Control: Analysis and Design, Second Edition. Wiley; 2005.